Shared Latent Coordinates and Multi-Observable Phase-Diagram Placement Yield Directly Comparable Mechanistic Fingerprints of Whole-Brain Dynamics

Julian Kędys[1]*, **Cezary Mazurek**[1]

[1]Department of Digital Medicine, Poznan Supercomputing and Networking Center, Polish Academy of Sciences
*jkedys@man.poznan.pl

Abstract

We present a methods-first framework that turns high-dimensional population neural recordings into directly comparable, mechanistic fingerprints at the level of individual subjects. Our pipeline (i) constructs population-universal, shared latent coordinates that align heterogeneous subjects into a common representational space; (ii) fits pairwise maximum-entropy (Ising) models on binarised latent trajectories with rigorous convergence- and uncertainty-diagnostics; (iii) performs energy-landscape analysis (ELA) to obtain interpretable minima, barriers and kinetic descriptors; and (iv) introduces a new, variance-balanced multi-observable phase-diagram analysis (PDA) that places many subjects - including systematically heterogeneous sub-groups - onto a shared Sherrington–Kirkpatrick (SK) reference surface with uncertainty, making cross-subject comparisons direct and faithful. In a cohort of rodent whole-brain imaging time series (third-party data under restricted access), our placement costs are typically 10^{-6}–10^{-4}, with tight bootstrap confidence regions and consistent ordering across pooled and subgroup references; estimated SK parameters fall in $\sigma \approx 0.155$–0.320, $\mu \approx -0.013$ to $+0.031$. The result is a compact, uncertainty-aware subject "fingerprint" comprising ELA and kinetic descriptors together with the subject's location on the phase diagram. This paper focuses on methodological reliability and cross-subject comparability; external replications on public datasets remain future work.

Introduction

Population neuroscience increasingly requires methods that *faithfully* compare brain dynamics across many heterogeneous subjects while remaining *mechanistically interpretable* (Robert and Escoufier 1976; Opper and Saad 2001; Ezaki et al. 2020; Macé et al. 2011; Deffieux, Demené, and Tanter 2021; Renaudin et al. 2022). Purely observational descriptors (e.g., simple power or correlation summaries) often fail to capture multi-stable structure and transition kinetics that are central to brain-state organisation (de Cheveigné et al. 2019; Metropolis et al. 1953; Becker and Karplus 1997; Watanabe et al. 2014). Conversely, subject-specific representational spaces can hinder direct cross-subject comparison of mechanistic models, motivating shared latent coordinates (Haxby et al. 2011).

We address this gap with a pipeline that first expresses all subjects in a **shared latent space** trained at the population level, then applies **physics-guided modelling** to produce **directly comparable** descriptors and a **multi-observable placement** on a shared phase diagram. The stitching of these steps is key: shared coordinates standardise feature semantics across individuals, enabling faithful subject-level ELA and a robust PDA objective that balances several observables with uncertainty.

Contributions:

- A robust procedure to build *population-universal shared latents* by aligning and synergistically fusing several population methods (Group PCA/ICA, SRM, MCCA) with stability checks (Calhoun et al. 2001).
- A rigorously diagnosed *pairwise maximum-entropy* (Ising) modelling stage with pseudo-likelihood and variational-Bayes estimators, posterior uncertainty and fit-quality assessments.
- A *variance-balanced multi-observable PDA* that yields *directly comparable* placements of many subjects onto a shared SK phase surface with bootstrap uncertainty.
- A compact, uncertainty-aware *mechanistic fingerprint* per subject: minima, barriers, kinetic descriptors (e.g., MFPTs, committors, spectral gap, Kemeny constant) and the phase location (μ, σ).

Related Work

Shared-representation learning across subjects has been pursued via SRM/MCCA/Group-PCA/ICA families (de Cheveigné et al. 2019; Kettenring 1971; Correa et al. 2010; Calhoun et al. 2001; Hyvärinen 1999; Kaiser 1958; Haxby et al. 2011). These approaches standardise feature semantics across individuals, improving sensitivity and enabling downstream comparisons across participants, tasks and datasets. In contrast to pipelines that analyse each participant in idiosyncratic spaces, we explicitly enforce *population-universal shared latents*, which makes subsequent ELA and PDA *directly comparable* across heterogeneous subjects.

Pairwise maximum-entropy/Ising modelling has a long history as a minimal-bias description of population activity, matching only first- and second-order moments while

remaining expressive (Jaynes 1957; Schneidman et al. 2006; Besag 1975; Ravikumar, Wainwright, and Lafferty 2010). In neuroimaging, Ising/PMEM parameters have underpinned both energy-landscape analysis and phase-diagram studies, linking macroscopic dynamics to statistical-physics observables (Watanabe et al. 2014; Edwards and Anderson 1975; Sherrington and Kirkpatrick 1975). Our design pairs a safeguarded pseudo-likelihood optimiser with a variational-Bayes route for uncertainty, reflecting practice in inverse Ising inference at scale while keeping a clear generative interpretation.

Energy-landscape analysis (ELA) characterises metastable structure, barriers and transition pathways in fitted PMEMs (Wales 2006; E and Vanden-Eijnden 2006; Becker and Karplus 1997). We follow the disconnectivity-graph framework and complement it with kinetic descriptors (committors, MFPTs, relaxation spectra and the Kemeny constant) derived from a single-spin-flip Markov chain.

Phase-diagram analysis (PDA) maps cohort dynamics to a reference SK surface. Prior work often intersected iso-curves of two observables (Ezaki et al. 2020) (typically χ_{SG} and χ_{uni}), which can be brittle when iso-curves are nearly parallel. We instead minimise a *variance-balanced, multi-observable* objective over $(m, q, \chi_{\mathrm{SG}}, \chi_{\mathrm{uni}})$ (optionally C), yielding smooth local bowls and a single well-posed optimum with uncertainty. Our use of *shared latents* is a key difference: it standardises the semantics of observables across individuals, enabling faithful, directly comparable placements and interpretable ELA descriptors in a common coordinate system.

Data Handling and ELA-Aware Preprocessing

We analyse multi-subject whole-brain time series. Because both ELA and Ising fitting rely on on/off switchings and co-activation structure, we adopt preprocessing designed to preserve the binarisation-relevant signal structure, removing nuisance trends and spikes while preserving threshold crossings.

Dataset summary (anonymised): Resting-state functional ultrasound (fUS) in $N{=}8$ mice (seven Cre-lox ASD models across four subtypes and one control); 54 bilateral regions (27 L/R pairs); two runs per mouse, 1494 frames each at TR ≈ 0.6 s; runs concatenated per subject; whole-brain coverage. We binarise shared-space latents per subject (median thresholds) and proceed with PMEM/ELA/PDA as described. These parameters are representative of the cohorts we analyse and are sufficient for replication of all results shown.

Notation: Let $x_{t,v}^{(i)}$ be the signal at time t and location/channel v for subject i. After projection into the consensus latent space we work with $s_{t,k}^{(i)}$, the k-th latent time course.

Preprocessing steps (seeded, configuration-driven):

1. **Robust de-spiking:** Identify outliers via a running MAD (median absolute deviation) filter and replace them with local robust estimates (window sizes specified in the config). This removes impulsive artefacts without shrinking genuine state transitions.
2. **Low-frequency trend handling:** Fit a low-order LOESS/LOWESS smoother (Cleveland 1979) to each raw channel and subtract it when (and only when) cross-validated residual reduction exceeds a user threshold. This corrects slow drifts while preserving segment endpoints that determine threshold crossings.
3. **Standardisation:** After population projection, standardise each latent to zero mean and unit variance within subject to avoid dominance by high-variance latents.
4. **Concordance checks:** Compute pre/post binarisation agreement for each latent (fraction of time points with identical binarised states under a common threshold rule). Flag or exclude subjects whose concordance falls below a configured threshold.

Binarisation: For each component k, threshold $s_{t,k}^{(i)}$ at a robust location θ_k (median unless stated) and map to spins

$$z_{t,k}^{(i)} = \mathrm{sign}\big(s_{t,k}^{(i)} - \theta_k\big) \in \{-1, +1\}.$$

Activity fractions and their temporal stability are monitored as sanity checks.

Reproducibility: All steps are deterministic given seeds. The run configuration (preprocessing windows, LOESS spans, gates, seeds) is saved per run to enable exact reproduction.

Population-Universal Shared Latent Coordinates

Let $X^{(i)} \in R^{T_i \times V}$ be subject-i observations. We construct K shared components via a multi-method procedure that aligns heterogeneous models into a common basis and fuses them with stability-aware weights.

Per-method estimation: We train population methods $m \in \{\text{Group PCA}, \text{Group ICA}, \text{SRM}, \text{MCCA}\}$ to obtain loadings $W_m \in R^{V \times K}$ and subject time courses $S_m^{(i)} \in R^{T_i \times K}$. Methods with stochastic elements (e.g., ICA) are run with multiple restarts.

Alignment to a reference: For each method m,

$$R_m^\star = \arg\min_{R_m} \ \|W_m R_m - W_{\mathrm{ref}}\|_F^2 \quad \text{s.t. } R_m^\top R_m = I,$$

followed by Hungarian matching across components and sign harmonisation (Schönemann 1966; Kuhn 1955). We ensure a clean one-to-one correspondence by inspecting the cross-method correlation matrices.

Synergy-weighted fusion: We form

$$W_\star = \sum_m \alpha_m \widetilde{W}_m, \qquad \alpha_m \geq 0, \ \sum_m \alpha_m = 1,$$

where $\widetilde{W}_m = W_m R_m^\star$ and α_m reflect method stability and cross-method agreement (high diagonal dominance $\Rightarrow$ larger α_m). Subject time courses are $S^{(i)} = X^{(i)} W_\star$.

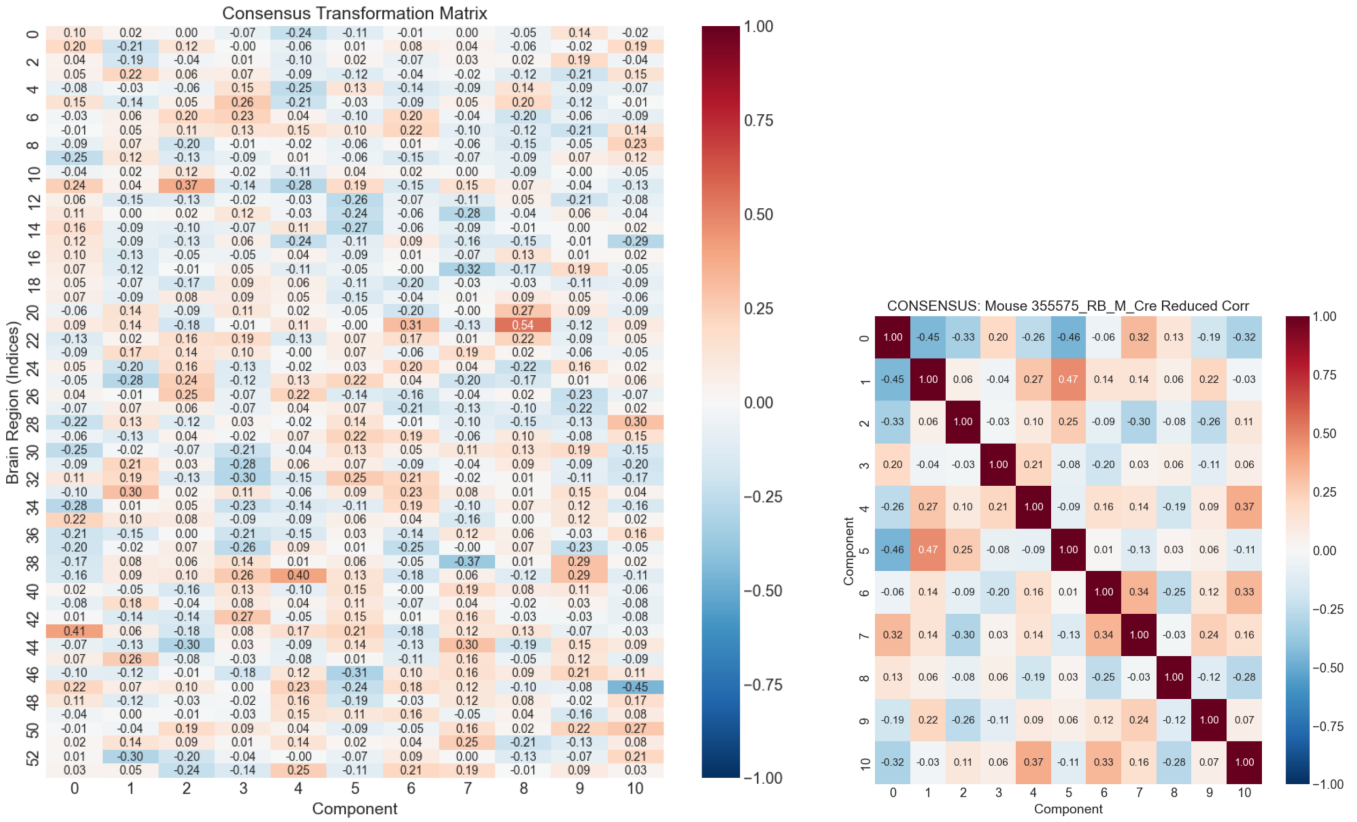

Figure 1: **Population-universal shared latent coordinates.** The **left** panel shows the consensus transformation mapping brain regions (rows) to population-shared components (columns), obtained by aligning Group-PCA/ICA, SRM and MCCA and fusing them with stability-aware weights (signs/orders harmonised). The **right** panel shows an example subject's reduced correlation matrix in the consensus space. By construction, the diagonal entries are 1; the informative signal is the faint off-diagonals, which indicate limited cross-component correlation (promoting orthogonality) and thus relatively little redundancy among latent time series. This shared basis preserves distinct dynamics while standardising features across subjects for downstream PMEM/ELA and PDA comparisons.

Stability diagnostics: We track (i) cross-subject reproducibility via mean absolute component correlations with permutation-derived nulls, (ii) cross-method agreement (diagonal structure), (iii) temporal trustworthiness/continuity of $S^{(i)}$ (Venna and Kaski 2006), and (iv) RV-coefficient stability across subsamples (Robert and Escoufier 1976). Fig. 1 visualises the consensus transformation and the reduced correlation structure in the shared space.

Pairwise Maximum-Entropy Modelling

For each subject we fit a pairwise MaxEnt (Ising) model to $z_t \in \{-1, +1\}^K$:

$$p(z \mid h, J) = \frac{1}{Z(h, J)} \exp\left(\sum_{k=1}^{K} h_k z_k + \frac{1}{2} \sum_{k \neq \ell} J_{k\ell} z_k z_\ell\right),$$

with $h \in R^K$ and symmetric $J \in R^{K \times K}$, $J_{k\ell} = J_{\ell k}$, $J_{kk} = 0$.

Pseudo-likelihood (PL): We maximise

$$\mathcal{L}_{\mathrm{PL}}(h, J) = \sum_{t=1}^{T} \sum_{k=1}^{K} \log \sigma\left(2 z_{t,k}\left(h_k + \sum_{\ell \neq k} J_{k\ell} z_{t,\ell}\right)\right),$$

where $\sigma(u) = 1/(1 + e^{-u})$, with L_2 regularisation and symmetry enforcement on J. Convergence is declared by relative changes in parameters and objective. We report moment-matching errors and tractable configuration probabilities for fit quality.

Variational Bayes (VB): With Gaussian priors $h \sim \mathcal{N}(0, \tau_h^{-1} I)$ and $\mathrm{vec}(J) \sim \mathcal{N}(0, \tau_J^{-1} I)$, we use a mean-field Gaussian $q(h, J)$ and maximise

$$\mathcal{L}_{\mathrm{VB}} = E_q[\log p(Z \mid h, J)] + E_q[\log p(h, J)] - E_q[\log q(h, J)].$$

We monitor monotone ELBO ascent, store posterior means/covariances (or diagonals) for uncertainty, and track an ARD spectrum on J. PL and VB point estimates are cross-checked for consistency. Fig. 2 summarises diagnostics.

Energy-Landscape Analysis (ELA)

Given (h, J), the energy of state z is

$$E(z) = -\sum_{k=1}^{K} h_k z_k - \frac{1}{2}\sum_{k\neq\ell} J_{k\ell} z_k z_\ell.$$

We enumerate or sample low-energy states to identify local minima and barrier heights, and we construct a disconnectivity graph (Wales 2006). Transition dynamics are defined via a single-spin-flip Markov chain (Metropolis or Glauber), yielding a transition matrix P (Metropolis et al. 1953; Kemeny and Snell 1960).

Minima, saddles and barriers: We locate minima by best-first search from observed states and refine by steepest-descent in energy. Pairwise barrier heights are estimated by constrained searches along low-energy paths (best path over a bounded neighbourhood). The resulting barrier matrix supports basin graph construction and the disconnectivity tree.

Kinetic descriptors: From P we compute:

- **Committors** $q_A(z)$ as the solution of a Dirichlet problem $(I - P)q_A = 0$ on transient states with $q_A = 1$ on A and $q_A = 0$ on B.
- **Mean first-passage times** (MFPTs) by solving Poisson equations $(I - P_{\mathcal{T}\mathcal{T}})m = \mathbf{1}$ on transient sets T.
- **Relaxation spectrum** $1 = \lambda_1 > \lambda_2 \geq \cdots$ and spectral gap $1 - \lambda_2$.
- **Kemeny constant** $K = \sum_{r=2}^{n} \frac{1}{1-\lambda_r}$ as a mixing summary.

Multi-Observable Phase-Diagram Placement (PDA)

We place each subject on a shared SK surface parameterised by (μ, σ), using multiple observables. Let $\widehat{O}_a$ denote empirical observables computed from the fitted subject model (with uncertainty), and $O_a^{\mathrm{SK}}(\mu, \sigma)$ their values on the precomputed SK surface. We consider

$$O \in \{m,\ q,\ \chi_{\mathrm{uni}},\ \chi_{\mathrm{SG}},\ C\}.$$

Variance-balanced objective:

$$(\mu^\star, \sigma^\star) = \arg\min_{\mu,\sigma} \sum_a w_a \big(\widehat{O}_a - O_a^{\mathrm{SK}}(\mu, \sigma)\big)^2 + \lambda_\mu \mu^2 + \lambda_\sigma \sigma^2,$$

with weights $w_a \propto 1/\widehat{\mathrm{Var}}(\widehat{O}_a)$ estimated by circular block bootstrap (block length B), normalised to $\sum_a w_a = 1$. Small ridge terms $(\lambda_\mu, \lambda_\sigma)$ stabilise boundary behaviour (Politis and Romano 1992).

Uncertainty on $(\mu^\star, \sigma^\star)$: We report either (i) the inverse Hessian of the objective at the optimum as a local covariance approximation, or (ii) empirical bootstrap ellipses obtained by re-estimating $(\mu^\star, \sigma^\star)$ over bootstrap resamples.

Computation: We perform a coarse grid search over (μ, σ) on the SK surface, followed by a local trust-region/quadratic fit around the best grid point. Gradients used in the local step are obtained by finite differences on $O_a^{\mathrm{SK}}(\mu, \sigma)$ (precomputed table with bilinear interpolation). Figs. 4–5 illustrate the objective landscape and cohort placements.

Results

Cohort and shared latents: Shared latents were stable across SRM/MCCA/Group-PCA/ICA; cross-method correlation matrices showed clean diagonals and no single-method dominance. Temporal trustworthiness/continuity metrics on projected trajectories were stable across subjects. Binarised activity fractions stayed within expected ranges over time.

Fit quality and uncertainty: For PMEM fits, pseudo-likelihood and VB estimators agreed within uncertainty. Diagnostics included: (i) moment-matching errors (means and pairwise correlations), (ii) empirical-vs-model configuration probabilities on tractable subsets, (iii) multi-information explained and KL-divergence reduction against independence baselines, and (iv) ELBO monotonicity for VB. Posterior s.d. on fields/couplings reflected magnitude ordering (larger $|J_{k\ell}|$ with smaller relative uncertainty).

Convergence-certified observables: Observables $(m, q, \chi_{\mathrm{SG}}, \chi_{\mathrm{uni}}, C)$ were estimated with multi-chain MCMC; we reported $\widehat{R}$ and effective sample sizes for chains (Vehtari et al. 2021). Across subjects, ESS exceeded conventional thresholds and $\widehat{R} \approx 1.00$–1.01 for monitored statistics.

Phase-diagram placements: The variance-balanced objective produced well-posed optima with low residuals (per-subject costs typically 10^{-6}–10^{-4}). Local cost surfaces were smooth and convex near the minimum. Estimated parameters covered $\sigma \approx 0.155$–0.320 and $\mu \approx -0.013$ to $+0.031$. Bootstrap ellipses around $(\mu^\star, \sigma^\star)$ were tight, and subgroup-specific vs pooled references preserved between-subject orderings, suggesting robust localisation rather than artefacts of the reference set.

Interpretable dynamics: ELA descriptors revealed small sets of recurrent minima with interpretable barrier structure. Descriptor panels summarised (a) one-step transition counts, (b) basin dwell/occupancy, (c) multi-step reachability (direct+indirect), and (d) escape-barrier distributions. We observed subtype-level patterns (e.g., concentrated vs distributed reachability; shifts in barrier modes), consistent with mechanistic differences in stability and switching propensity rather than mere coordinate effects.

Comparisons to iso-curve intersections: Relative to classic two-iso-curve intersections, our objective avoids ambiguous placements under near-parallel iso-curves, fits multiple observables *jointly*, and propagates uncertainty coherently. In practice this eliminated multi-solution edge cases and produced smoother placement trajectories under resampling.

Ablations, Robustness, and Quality-Control

Shared-latent ablations: Leave-one-method-out fusions (SRM/MCCA/Group-PCA/ICA) preserve component identities; we quantify stability via RV-coefficients against the full model and by diagonality of cross-method correlation matrices.

Binarisation sensitivity: Median vs. mean thresholds yield consistent activity fractions; we report paired differences and bootstrap CIs, and gate on excessive shifts in ELA minima counts.

Ising estimators: PL and VB estimates agree within posterior uncertainty; ARD spectra indicate effectively sparse couplings. We gate on PL relative parameter/objective change and VB ELBO monotonicity.

Null thresholds and false-structure gates: Permutation-based nulls (time shuffles within latents) define thresholds for spurious ELA minima and unstable components; configurations failing these are rejected.

Bootstrap uncertainty: Circular block bootstrap over time provides uncertainty for observables and PDA placements; we report (μ, σ) ellipses and check for pathological multimodality (gated by mixture diagnostics).

Reproducibility, Data, and Code Availability

Runs are deterministic and configuration-driven (single YAML file controlling seeds, preprocessing options, model hyper-parameters, grid resolutions for SK surfaces and bootstrap settings). Software versions and environment specifications are recorded automatically, and per-run quality-control reports (convergence diagnostics, fit indices, null-threshold checks) are produced.

Data: The datasets analysed are under third-party agreements and cannot be publicly released. We provide key preprocessing details and parameters to enable replication on public data.

Code: No public code repository accompanies this paper. The pipeline implementation is available from the corresponding author upon reasonable request. The methodology is documented at the level of detail sufficient for independent reimplementation.

Limitations and Future Directions

Scope: Our present focus is methodological on small-N external data. We plan broader validations across public datasets and modalities (fMRI/EEG/MEG), with harmonised shared-latent front-ends and ablations (SRM vs. MCCA vs. Group PCA/ICA) for concordant (μ, σ) orderings.

Objective extensions: We are extending the PDA objective with specific heat C and near-criticality indices, and formalising block-bootstrap strategies (block-length selection, overlapping vs non-overlapping) for autocorrelated series (Politis and White 2004).

Software Distribution and Reproducibility: We are packaging a reference environment (container/conda) with example notebooks, standard benchmarking panels (fit vs nulls, runtime/memory vs baselines, stress tests), and detailed provenance logs. This supports peer validation and integration in automated analysis workflows.

Phenotyping potential: Because the outputs are interpretable and cohort-comparable, the framework supports phenotype stratification, response-heterogeneity analysis, and cross-condition comparisons—especially relevant for neurodevelopmental cohorts where healthy baselines may be unavailable.

Ethics Statement

All procedures involving animal data were approved by the relevant institutional committees and complied with applicable regulations. No new data were collected for this study; we analysed existing restricted-access datasets under appropriate agreements.

Acknowledgements

We thank Professor Takao Hensch (Harvard University and Boston Children's Hospital), who motivated the original line of inquiry that led to this study and whose laboratory provided the functional ultrasound dataset analysed here. We are also grateful to Professor Takamitsu Watanabe (University of Tokyo) for hosting a formative research internship at the International Research Center for Neurointelligence (WPI-IRCN) and for his pioneering work on energy-landscape analysis of neural data, which provided essential methodological foundations for this study.

References

Becker, O. M.; and Karplus, M. 1997. The Topology of Multidimensional Potential Energy Surfaces: Theory and Application to Peptide Structure and Kinetics. *The Journal of Chemical Physics*, 106(4): 1495–1517.

Besag, J. 1975. Statistical Analysis of Non-Lattice Data. *Journal of the Royal Statistical Society. Series D (The Statistician)*, 24(3): 179–195.

Calhoun, V. D.; Adali, T.; Pearlson, G. D.; and Pekar, J. J. 2001. A Method for Making Group Inferences from Functional MRI Data Using Independent Component Analysis. *Human Brain Mapping*, 14(3): 140–151.

Cleveland, W. S. 1979. Robust Locally Weighted Regression and Smoothing Scatterplots. *Journal of the American Statistical Association*, 74(368): 829–836.

Correa, N. M.; Eichele, T.; Adalı, T.; Li, Y.-O.; and Calhoun, V. D. 2010. Multi-Set Canonical Correlation Analysis for the Fusion of Concurrent Single Trial ERP and Functional MRI. *NeuroImage*, 50(4): 1438–1445.

de Cheveigné, A.; Di Liberto, G. M.; Arzounian, D.; Wong, D. D. E.; Hjortkjær, J.; Fuglsang, S.; and Parra, L. C. 2019. Multiway Canonical Correlation Analysis of Brain Data. *NeuroImage*, 186: 728–740.

Deffieux, T.; Demené, C.; and Tanter, M. 2021. Functional Ultrasound Imaging: A New Imaging Modality for Neuroscience. *Neuroscience*, 474: 110–121.

E, W.; and Vanden-Eijnden, E. 2006. Towards a Theory of Transition Paths. *Journal of Statistical Physics*, 123(3): 503–523.

Edwards, S. F.; and Anderson, P. W. 1975. Theory of Spin Glasses. *Journal of Physics F: Metal Physics*, 5(5): 965–974.

Ezaki, T.; Fonseca dos Reis, E.; Watanabe, T.; Sakaki, M.; and Masuda, N. 2020. Closer to Critical Resting-State Neural Dynamics in Individuals with Higher Fluid Intelligence. *Communications Biology*, 3(1): 52.

Haxby, J. V.; Guntupalli, J. S.; Connolly, A. C.; Halchenko, Y. O.; Conroy, B. R.; Gobbini, M. I.; Hanke, M.; and Ramadge, P. J. 2011. A Common, High-Dimensional Model of the Representational Space in Human Ventral Temporal Cortex. *Neuron*, 72(2): 404–416.

Hyvärinen, A. 1999. Fast and Robust Fixed-Point Algorithms for Independent Component Analysis. *IEEE Transactions on Neural Networks*, 10(3): 626–634.

Jaynes, E. T. 1957. Information Theory and Statistical Mechanics. *Physical Review*, 106: 620–630.

Kaiser, H. F. 1958. The Varimax Criterion for Analytic Rotation in Factor Analysis. *Psychometrika*, 23(3): 187–200.

Kemeny, J. G.; and Snell, J. L. 1960. *Finite Markov Chains*. Van Nostrand.

Kettenring, J. R. 1971. Canonical Analysis of Several Sets of Variables. *Biometrika*, 58(3): 433–451.

Kuhn, H. W. 1955. The Hungarian Method for the Assignment Problem. *Naval Research Logistics Quarterly*, 2(1-2): 83–97.

Macé, É.; Montaldo, G.; Cohen, I.; Baulac, M.; Fink, M.; and Tanter, M. 2011. Functional Ultrasound Imaging of the Brain. *Nature Methods*, 8(8): 662–664.

Metropolis, N.; Rosenbluth, A. W.; Rosenbluth, M. N.; Teller, A. H.; and Teller, E. 1953. Equation of State Calculations by Fast Computing Machines. *The Journal of Chemical Physics*, 21(6): 1087–1092.

Opper, M.; and Saad, D., eds. 2001. *Advanced Mean Field Methods: Theory and Practice*. MIT Press.

Politis, D. N.; and Romano, J. P. 1992. A Circular Block-Resampling Procedure for Stationary Data. In *Exploring the Limits of Bootstrap*. Wiley.

Politis, D. N.; and White, H. 2004. Automatic Block-Length Selection for the Dependent Bootstrap. *Econometric Reviews*, 23(1): 53–70.

Ravikumar, P.; Wainwright, M. J.; and Lafferty, J. D. 2010. High-Dimensional Ising Model Selection Using ℓ_1-Regularized Logistic Regression. *The Annals of Statistics*, 38(3): 1287–1319.

Renaudin, N.; Demené, C.; Dizeux, A.; Ialy-Radio, N.; Tanter, M.; and Pezet, S. 2022. Functional Ultrasound Localization Microscopy Reveals Brain-Wide Neurovascular Activity on a Microscopic Scale. *Nature Methods*, 19: 1004–1014.

Robert, P.; and Escoufier, Y. 1976. A Unifying Tool for Linear Multivariate Statistical Methods: The RV-Coefficient. *Journal of the Royal Statistical Society. Series C (Applied Statistics)*, 25(3): 257–265.

Schneidman, E.; Berry, M. J.; Segev, R.; and Bialek, W. 2006. Weak Pairwise Correlations Imply Strongly Correlated Network States in a Neural Population. *Nature*, 440(7087): 1007–1012.

Schönemann, P. H. 1966. A Generalized Solution of the Orthogonal Procrustes Problem. *Psychometrika*, 31(1): 1–10.

Sherrington, D.; and Kirkpatrick, S. 1975. Solvable Model of a Spin-Glass. *Physical Review Letters*, 35: 1792–1796.

Vehtari, A.; Gelman, A.; Simpson, D.; Carpenter, B.; and Bürkner, P.-C. 2021. Rank-Normalization, Folding, and Localization: An Improved $\hat{R}$ for Assessing Convergence of MCMC (with Discussion). *Bayesian Analysis*, 16(2): 667–718.

Venna, J.; and Kaski, S. 2006. Local Multidimensional Scaling. *Neural Networks*, 19(6): 889–899.

Wales, D. J. 2006. Energy Landscapes: Calculating Pathways and Rates. *International Reviews in Physical Chemistry*, 25(1-2): 237–282.

Watanabe, T.; Hirose, S.; Wada, H.; Imai, Y.; Machida, T.; Shirouzu, I.; Konishi, S.; Miyashita, Y.; and Masuda, N. 2014. Energy Landscapes of Resting-State Brain Networks. *Frontiers in Neuroinformatics*, 8: 12.

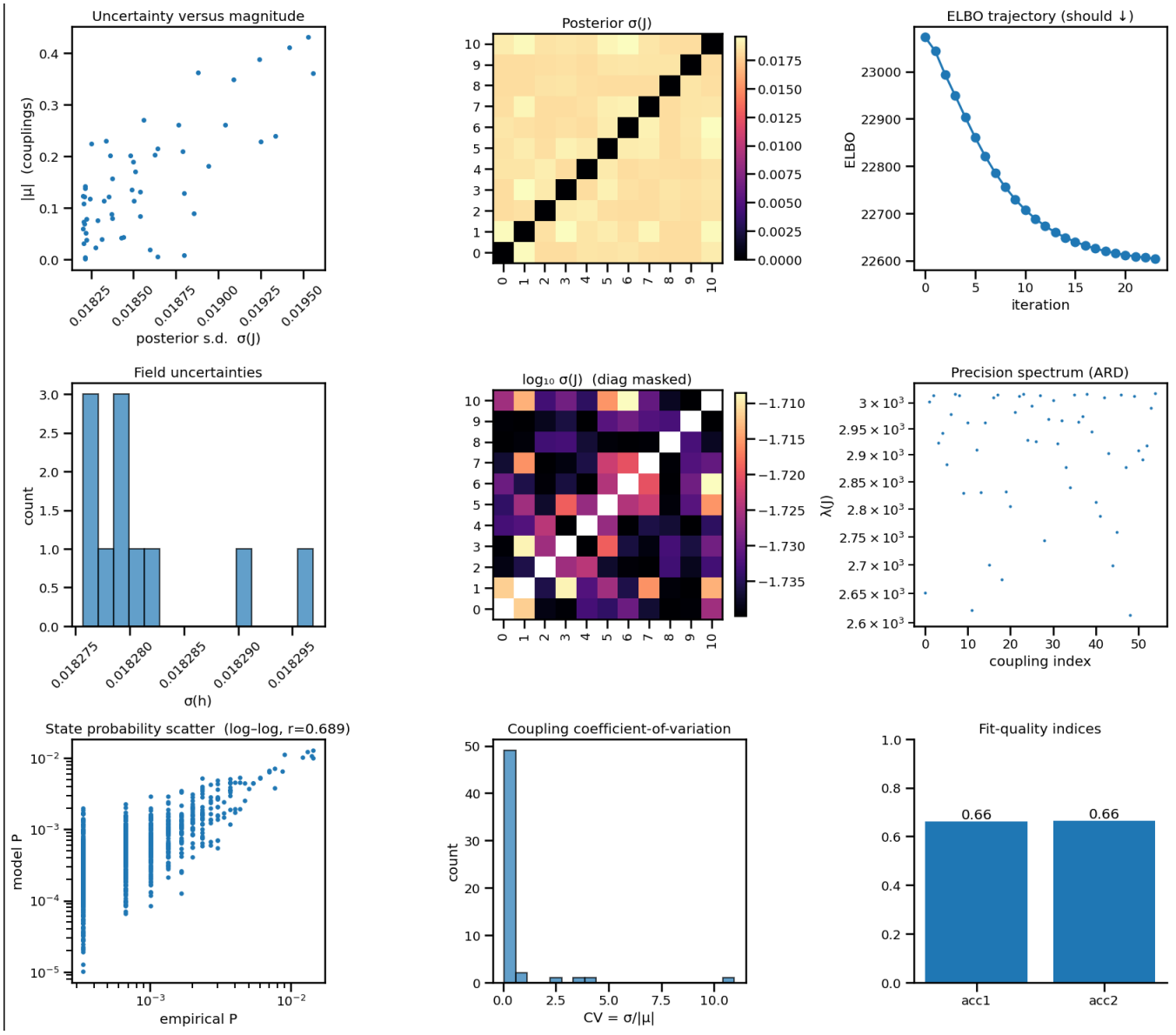

Figure 2: **Variational–Bayes posterior diagnostics and model fit for the pairwise Ising (PMEM). (a)** Scatter of parameter magnitude versus posterior uncertainty for couplings: points show $|J_{ij}|$ against posterior standard deviation $\sigma(J_{ij})$; larger magnitudes tend to have smaller uncertainty. **(b)** Heat map of coupling uncertainties $\sigma(J_{ij})$ (diagonal masked); warmer colours denote higher posterior s.d. across pairs (i, j). **(c)** Evidence lower bound (ELBO) trajectory across iterations. Because we plot the negative ELBO, the curve should decrease monotonically as the VB updates converge. **(d)** Histogram of field uncertainties $\sigma(h_i)$ across regions/nodes. **(e)** $\log_{10}\sigma(J_{ij})$ with the diagonal masked, highlighting orders-of-magnitude spread in pairwise uncertainty. **(f)** Automatic relevance determination (ARD) precision spectrum λ: larger λ indicates stronger shrinkage (less relevant parameters). **(g)** State-probability agreement on log–log axes: model probabilities $P_{\text{model}}(s)$ versus empirical $P_{\text{emp}}(s)$; points near the identity line indicate better fit (reported Pearson r in title). **(h)** Coefficient of variation for couplings, $\text{CV} = \sigma(J_{ij})/|J_{ij}|$; most parameters exhibit small relative uncertainty (bars near low CV). **(i)** Fit-quality indices summarising model performance: entropy-based "accuracy" and KL-based improvement (here shown as acc1 and acc2); values closer to 1 indicate stronger improvements over the independent model.

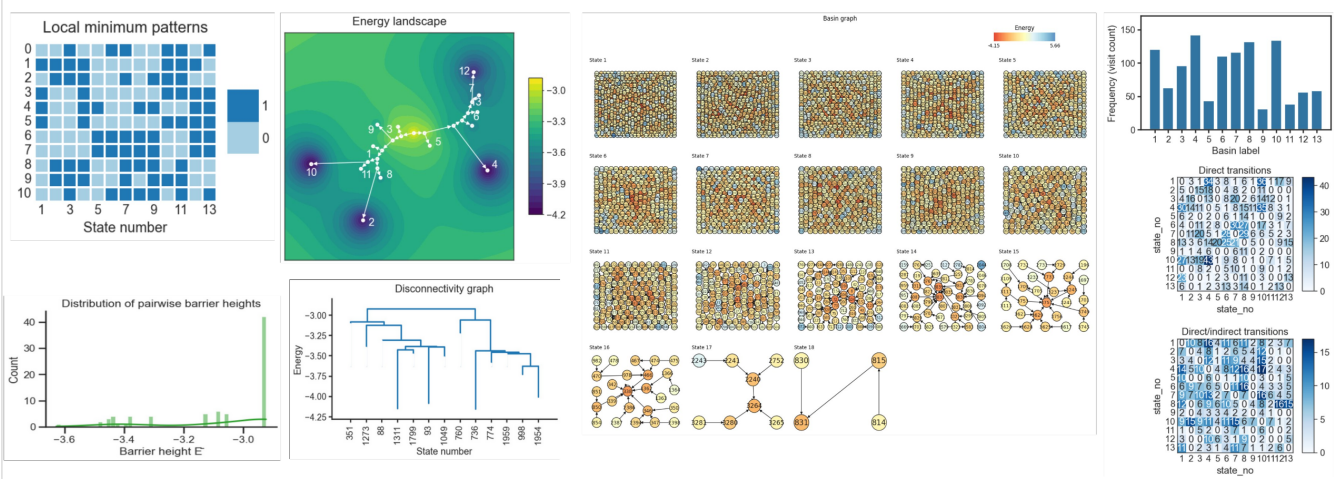

Figure 3: **Key deliverables of Energy–Landscape Analysis (ELA) for a fitted pairwise Ising/PMEM.** We model binary brain states $\mathbf{s} \in \{-1, 1\}^n$ with energy $E(\mathbf{s}) = -\mathbf{h}^\top \mathbf{s} - \frac{1}{2}\mathbf{s}^\top J\mathbf{s}$. Local minima ("attractors") are states that are not lowered by any single–spin flip; a *basin* is the set of states that descend to the same attractor under single–flip downhill dynamics. Adjacency is Hamming distance 1. Barrier heights between basins α, β are computed from a bottleneck search on the full 2^n-state graph and reported as $\Delta E_{\alpha\beta} = D_{\alpha\beta} - \max\{E_\alpha, E_\beta\}$, where D is the disconnectivity matrix and E_α is the attractor energy. **(a) Local–minimum patterns.** Binary spin patterns of all attractor states (columns ordered by identifier; rows are nodes/regions). Dark/light encode 1 vs. 0 (the underlying ± 1 states recoded to $\{0, 1\}$ for display). This reveals which subsystems flip across minima. **(b) Energy landscape.** A 2D projection of the energy surface with contours/heatmap (colour bar in energy units). Labelled dots mark attractor locations; dotted paths indicate representative downhill/transition trajectories between minima via saddles. **(c) Basin graphs.** One panel per basin: nodes are discrete states within the basin, coloured by energy; edges connect Hamming–1 neighbours along downhill directions. **(d) Dwell frequencies.** Histogram of visit counts per basin freq_α obtained by run–length encoding the time series after mapping each frame to its basin label (unassigned frames are excluded). This quantifies empirical stability/occupancy. **(e) Direct transitions $T^{(1)}$.** Heatmap of one–step transitions between consecutive dwell runs, with entry $T^{(1)}_{\alpha\beta}$ the number of $\alpha \to \beta$ moves ($\alpha \neq \beta$). Self–loops are omitted to emphasise inter–basin moves. **(f) Direct/indirect transitions $T^{(2)}$.** Two–step counts ($\alpha \to \gamma \to \beta$, $\alpha \neq \beta$) summarising short indirect traffic between basins. **(g) Barrier distribution.** Empirical distribution of pairwise barrier heights $\Delta E_{\alpha\beta}$ across all basin pairs, indicating how separated the attractors are by the landscape topology. **(h) Disconnectivity graph.** Dendrogram of basins (leaves labelled by attractor/state number; vertical axis is energy). Branch heights reflect $D_{\alpha\beta}$, revealing the hierarchical organisation of minima and the saddle structure that separates them.

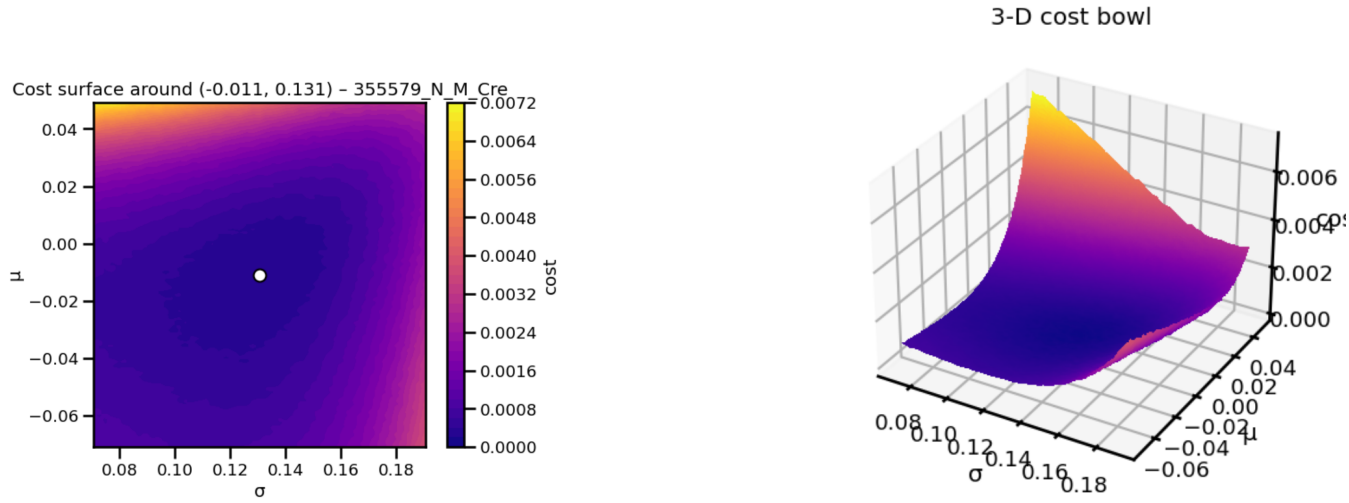

Figure 4: **Phase-diagram placement objective landscape. Left:** Two-dimensional cost surface around the optimum in (μ, σ) space; the white dot marks the estimated parameters. **Right:** Three-dimensional view of the same landscape, highlighting a well-conditioned "bowl" near the minimum. Both indicate stable, identifiable placement under the multi-observable objective.

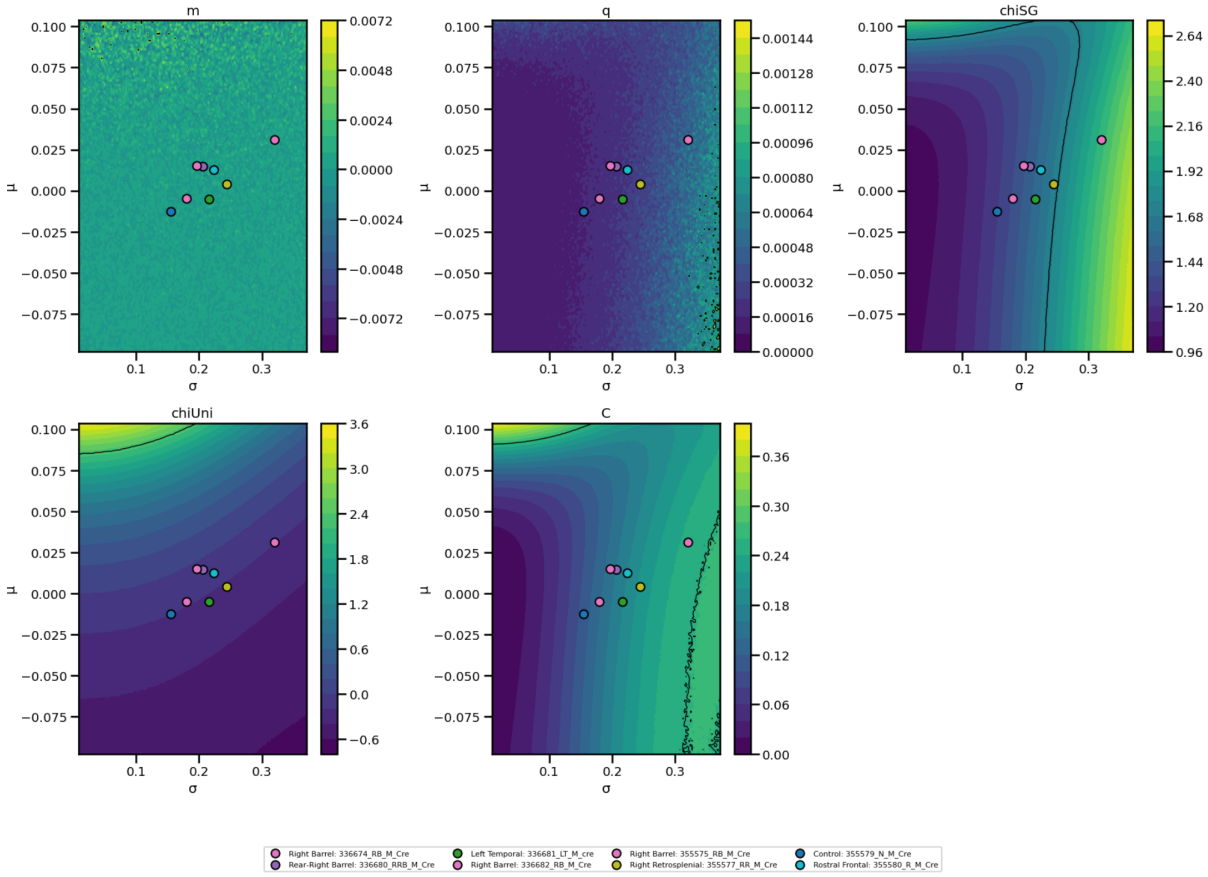

Figure 5: **Phase–Diagram Analysis (PDA): cohort placement and observable fields on the (σ, μ) plane.** Each panel shows a filled–contour map of a PDA observable evaluated under the fitted pairwise Ising model, as a function of network heterogeneity σ (x-axis) and mean coupling μ (y-axis). Coloured markers indicate the cohort sessions (same markers in all panels). Black/steep isolines mark regions where the observable varies rapidly; peaks in χ_{SG}, χ_{uni}, and C indicate proximity to phase boundaries. **Top row:** m (magnetisation), q (spin-glass order), and χ_{SG} (spin-glass susceptibility). **Bottom row:** χ_{uni} (uniform susceptibility) and C (specific heat). High values of χ_{SG}, χ_{uni}, or C correspond to increased sensitivity and richer fluctuations; low values indicate quiescent, stable dynamics. **PDA axes (interpretation).** σ - *network heterogeneity*: spread of coupling strengths across regions; higher σ means a few strong links dominate, lower σ means couplings are more even. μ - *net coupling / excitation–inhibition balance*: mean effective coupling; higher μ implies regions tend to co-activate (more cooperative), lower μ implies more independent/decoupled activity. **Key PDA observables (what the colour encodes).** m - *magnetisation*: whole-brain activation bias (overall "on" vs "off"); large $|m|$ indicates sustained hypo- or hyper-activation; $m \approx 0$ is balanced. q - *spin-glass order*: stability/rigidity of activation patterns; high q = rigid/repetitive, low q = flexible/variable. χ_{SG} - *spin-glass susceptibility*: sensitivity to *local* nudges (perturbing only some regions); high χ_{SG} = large reconfiguration from small local tweaks. χ_{uni} - *uniform susceptibility*: sensitivity to a *global* nudge (equal perturbation to all regions); high χ_{uni} = strong, coherent whole-brain shift. C - *specific heat / energy fluctuation*: variance of model energy across configurations; high C = many competing states and rich fluctuations near a phase boundary, low C = few configurations and quiescent/stable dynamics.